ADVANCED MATERIALS
www.advmat.de

Hierarchically Porous Carbons with Highly Curved Surfaces for Hosting Single Metal FeN_4 Sites as Outstanding Oxygen Reduction Catalysts

Guangbo Chen, Ruihu Lu, Chenzhao Li, Jianmin Yu, Xiaodong Li, Lingmei Ni, Qi Zhang, Guangqi Zhu, Shengwen Liu, Jiaxu Zhang, Ulrike I. Kramm, Yan Zhao, Gang Wu,* Jian Xie,* and Xinliang Feng**

Iron–nitrogen–carbon (Fe–N–C) materials have emerged as a promising alternative to platinum-group metals for catalyzing the oxygen reduction reaction (ORR) in proton-exchange-membrane fuel cells. However, their low intrinsic activity and stability are major impediments. Herein, an Fe–N–C electrocatalyst with dense FeN_4 sites on hierarchically porous carbons with highly curved surfaces (denoted as FeN_4-*hc*C) is reported. The FeN_4-*hc*C catalyst displays exceptional ORR activity in acidic media, with a high half-wave potential of 0.85 V (versus reversible hydrogen electrode) in 0.5 M H_2SO_4. When integrated into a membrane electrode assembly, the corresponding cathode displays a high maximum peak power density of 0.592 W cm^{-2} and demonstrates operating durability over 30 000 cycles under harsh H_2/air conditions, outperforming previously reported Fe–N–C electrocatalysts. These experimental and theoretical studies suggest that the curved carbon support fine-tunes the local coordination environment, lowers the energies of the Fe d-band centers, and inhibits the adsorption of oxygenated species, which can enhance the ORR activity and stability. This work provides new insight into the carbon nanostructure–activity correlation for ORR catalysis. It also offers a new approach to designing advanced single-metal-site catalysts for energy-conversion applications.

1. Introduction

Electrochemical energy conversion technologies, such as proton-exchange-membrane fuel cells (PEMFCs), are among the most sustainable energy devices available for reducing our reliance on fossil fuels and eliminating environmental concerns.[1–3] The electrocatalytic oxygen reduction reaction (ORR) is an indispensable process occurring at the cathodes of PEMFCs, and it largely determines the efficiencies and performance of such devices.[4–11] Currently, platinum-group metals (PGMs) are the most efficient catalysts for catalyzing the sluggish ORR kinetics because they have the appropriate adsorption strength for O-containing intermediates.[12] Unfortunately, the prohibitive costs, scarcities, and poor durability of these PGM catalysts seriously limit their widespread application in practical energy devices.[13–16]

Among the different PGM-free electrocatalysts, atomically dispersed iron–nitrogen–carbon (Fe–N–C) nanomaterials have emerged as prospective candidates for PEMFCs due to their impressive ORR performance in acidic media.[17–23] The single metal iron-coordinated nitrogen (FeN_4) sites embedded in the carbon matrix were identified as the active centers for catalyzing the ORR process.[24–33] Unfortunately, the adsorption strengths of the ORR intermediates (i.e., O* and OH*) on the FeN_4 site were still too strong compared to those for Pt, inhibiting their desorption and

G. Chen, X. Li, J. Zhang, X. Feng
Center for Advancing Electronics Dresden (Cfaed) and Faculty of Chemistry and Food Chemistry
Technische Universität Dresden
01062 Dresden, Germany
E-mail: xinliang.feng@tu-dresden.de

The ORCID identification number(s) for the author(s) of this article can be found under https://doi.org/10.1002/adma.202300907

DOI: 10.1002/adma.202300907

R. Lu, Y. Zhao
State Key Laboratory of Silicate Materials for Architectures
International School of Materials Science and Engineering
Wuhan University of Technology
Wuhan 430070, P. R. China
E-mail: yan2000@whut.edu.cn

C. Li, Q. Zhang, G. Zhu, J. Xie
Department of Mechanical and Energy Engineering
Purdue School of Engineering and Technology
Indiana University–Purdue University
Indianapolis, IN 46202, USA
E-mail: jianxie@iupui.edu

C. Li
School of Mechanical Engineering
Purdue University
West Lafayette, IN 47907, USA

conversion and thus limiting the overall ORR activity.[34,35] In addition, the insufficient long-term durability of the reported Fe–N–C materials also limits practical application.[36] During the last decade, numerous approaches have been explored to weaken the interactions of O*/OH* with the FeN_4 site and to improve the intrinsic ORR activities of Fe–N–C materials.[37] The typical methods used are the construction of edge-carbon host FeN_4 sites, preparation of FeN_4 sites within the micropores, and doping with other light heteroatoms (e.g., sulfur (S) or phosphorus (P)).[38–40] These strategies introduced defects into the carbon skeleton, resulting in stability loss during long-term operation.[41] Improving the degree of graphitization generally improves stability; however, the intrinsic activity was still not satisfactory.[42,43] Thus, the exploration of advanced carbon nanostructures is essential for simultaneously promoting the intrinsic activities of the FeN_4 sites and improving the durability of the Fe–N–C materials.

Herein, we report a novel Fe–N–C electrocatalyst with dense FeN_4 sites on hierarchically porous carbons with highly curved surfaces (denoted as FeN_4-*hc*C). FeN_4-*hc*C was prepared by pyrolysis of a surfactant poly(ethylene oxide)–poly(propylene oxide)–poly(ethylene oxide) (PEO_{20}–PPO_{70}–PEO_{20} (P123))-modified Fe-doped zeolitic imidazolate framework-8 (Fe-ZIF-8) precursor (P123@Fe-ZIF-8). During the pyrolysis process, the introduction of P123 with the Fe-ZIF-8 led to the formation of onion-like nanocarbons with plentiful curved carbon surfaces that decorated the ZIF-8-derived polyhedral carbons. The resultant FeN_4-*hc*C showed a highly curved carbon surface, a large surface area (733.9 $m^2\ g^{-1}$), and a high Fe content (1.15 wt%) associated with single sites. In a 0.5 M H_2SO_4 electrolyte, the prepared FeN_4-*hc*C displayed excellent ORR performance with a half-wave potential ($E_{1/2}$) of 0.85 V versus the reversible hydrogen electrode (RHE), surpassing that of FeN_4-C pyrolyzed without P123 ($E_{1/2}$ = 0.82 V) and approaching that of the Pt/C benchmark ($E_{1/2}$ = 0.86 V in 0.1 M $HClO_4$). We also integrated FeN_4-*hc*C as the cathode catalyst in a 1.0 bar H_2–O_2 PEMFC and achieved a current density of 26.9 mA cm^{-2} at 0.9 $V_{iR\text{-}free}$ (internal resistance compensated voltage). In a practical 1.0 bar H_2–air cell, the FeN_4-*hc*C generated a peak power density of 0.592 W cm^{-2} and showed promising durability. The overall PEMFC performance (mass activity, defined as the current density at 0.9 $V_{iR\text{-}free}$ in H_2–O_2, and the peak power density and stability in H_2–air) of FeN_4-*hc*C outperformed those of the reported Fe–N–C components. Density functional theory (DFT) calculations suggested that the curved carbon surface altered the electronic structure of the single FeN_4 sites by lowering the energies of the Fe d-band centers, weakening the interactions with OH* and promoting the intrinsic ORR activity. DFT calculations suggested that a carbon curvature is an efficacious tool for tuning the single Fe sites in Fe–N–C materials for ORR activity and stability.

2. Results and Discussion

As schematically illustrated in **Figure 1**a, FeN_4-*hc*C was prepared by using P123-mediated pyrolysis. First, P123 (2 g) was introduced in situ during the synthesis of the Fe-ZIF-8 by adding iron nitrate nonahydrate (60 mg) and zinc nitrate hexahydrate together (2.97 g) with 2-methylimidazole (2-MeIm, 3.40 g) in 300 mL of methanol, thus forming the P123@Fe-ZIF-8 composite. Second, the obtained P123@Fe-ZIF-8 powder was heated at 1100 °C for 1 h with a heating rate of 40 °C min^{-1} under a flowing argon (Ar) atmosphere, which yielded FeN_4-*hc*C. The synthetic details are provided in the Supporting Information. The hydrocarbon networks of ZIF-8 were carbonized to form a porous nitrogen-doped carbon matrix, while the doped Fe complexes were converted into atomically dispersed FeN_4 sites.[44] As displayed in Figure S1 (Supporting Information), the P123/Fe-ZIF-8 nanocrystals displayed defined rhombic dodecahedral shapes with particle sizes of ≈100 nm. X-ray diffraction (XRD) analyses provided identical diffraction patterns for ZIF-8, Fe-ZIF-8, and P123/Fe-ZIF-8 (Figure S2, Supporting Information), implying that the introduction of P123 and/or Fe ions did not influence the crystalline structure of the ZIF-8. The Fe content in P123@Fe-ZIF-8 is 0.22 wt% as determined by inductively coupled plasma-optical emission spectroscopy (ICP-OES) measurements. The Fe in P123@Fe-ZIF-8 is in 3+ oxidation state,[44] as revealed by X-ray photoelectron spectroscopy (XPS) analysis (Figure S3, Supporting Information). The P123 content in P123@Fe-ZIF-8 is estimated to be 29.1 wt%, according to the thermogravimetric analysis (TGA) (Figure S4, Supporting Information). For comparison, a FeN_4-C material was prepared by using an identical procedure but without employing P123.

The XRD technique was first employed to gather structural details for FeN_4-C and FeN_4-*hc*C. As depicted in Figure S5 (Supporting Information), FeN_4-C and FeN_4-*hc*C showed two peaks at ≈24.3° and ≈43.7°, corresponding to the (002) and (101) facets of graphitic carbon, respectively.[45] No diffraction peaks related to crystalline Fe species (e.g., Fe, Fe_3C, or Fe_3N nanoparticles) were observed. Scanning electron microscopy (SEM) and transmission electron microscopy (TEM) were then utilized to examine the morphologies of FeN_4-C and FeN_4-*hc*C. As shown in Figure 1b,c and in Figure S6 (Supporting Information), FeN_4-C and FeN_4-*hc*C inherited the morphology of ZIF-8, showing a polyhedral structure with particle sizes of ≈100 nm. For both FeN_4-C and FeN_4-*hc*C, no Fe-containing nanoparticles (e.g., Fe and/or Fe_3C) were identified in the TEM and high-angle annular dark-field scanning TEM (HAADF-STEM) images. The related elemental mapping images indicated homogeneous distributions of Fe, C, and N elements on the FeN_4-*hc*C and FeN_4-C

J. Yu
Key Laboratory of Photochemical Conversion and Optoelectronic Materials
Technical Institute of Physics and Chemistry
Chinese Academy of Sciences
Beijing 100190, P. R. China
X. Li, X. Feng
Department of Synthetic Materials and Functional Devices
Max Planck Institute of Microstructure Physics
D-06120 Halle (Saale), Germany
L. Ni, U. I. Kramm
Department of Chemistry
Eduard-Zintl Insitute of Physical and Inorganic Chemistry
TU Darmstadt
D-64287 Darmstadt, Germany
S. Liu, G. Wu
Department of Chemical and Biological Engineering
University at Buffalo
The State University of New York
Buffalo, NY 14260, USA
E-mail: gangwu@buffalo.edu

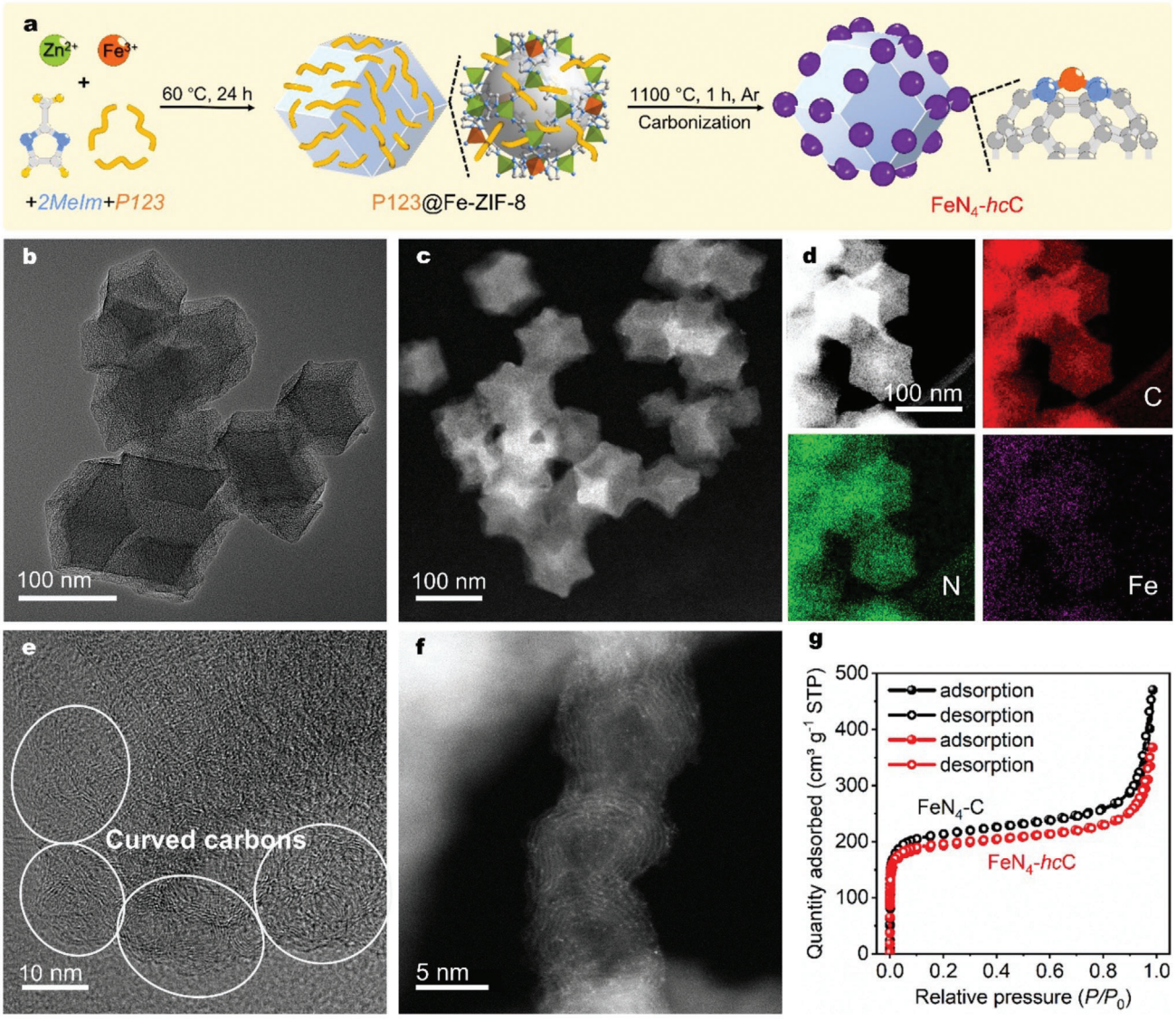

Figure 1. a) Schematic illustration for the synthesis of FeN_4-*hc*C. b) TEM, c) HAADF-STEM images, d) HAADF-STEM, and the corresponding elemental images showing the distributions of C (red), N (green), and Fe (purple). e) High-resolution TEM and f) atomic-resolution HAADF-STEM images of FeN_4-*hc*C. g) N_2 adsorption/desorption isotherms for FeN_4-C and FeN_4-*hc*C.

(Figure 1d; Figure S7c, Supporting Information). Unlike FeN_4-C catalyst showing well-defined polyhedral particles with distinct edges and faces (Figure S7, Supporting Information), abundant onion-like carbons with diameters of ≈9 nm were observed on the surfaces of the polyhedral particles in FeN_4-*hc*C (Figure 1e,f; Figure S8, Supporting Information). These results indicated that the P123 copolymer effectively induced the formation of unique onion-like carbon nanostructures during the pyrolysis process.[46] The curvature (c, $c = 1/R$, R refers to the radius of the sphere) of the onion-like carbon was calculated to be ≈0.023. Control experiments suggested that the curved carbons were from Fe-ZIF-8 rather than P123 (Figure S9, Supporting Information). Aberration-corrected HAADF-STEM images (Figure 1f; Figure S8d, Supporting Information) showed abundant bright single dots on both the polyhedral carbon particles and the onion-like carbons, indicating the presence of high-density single Fe sites in FeN_4-*hc*C. For comparison, P123@Fe-ZIF-8 with different P123 contents (22.8 and 32.7 wt%) were also prepared by the similar approach, while using different dosages of P123 in the synthetic process (i.e., 1.5 and 2.5 g, respectively). The carbonized materials were denoted as FeN_4-*hc*C-1.5, and FeN_4-*hc*C-2.5, respectively (Figure S10a, Supporting Information). The high-resolution TEM (HRTEM) images showed that with the increase of the P123 content in the synthesis process, the content of curved carbons increases (Figure S10b–d, Supporting Information). These results indicated the critical role of the P123 in the formation of curved carbons. To further investigate the role of P123, we pyrolyzed Fe-ZIF-8 and P123@Fe-ZIF-8 at different temperatures (500–1100 °C). As shown in Figure S11 (Supporting Information), the carbon was formed at ≈600 °C, as evidenced

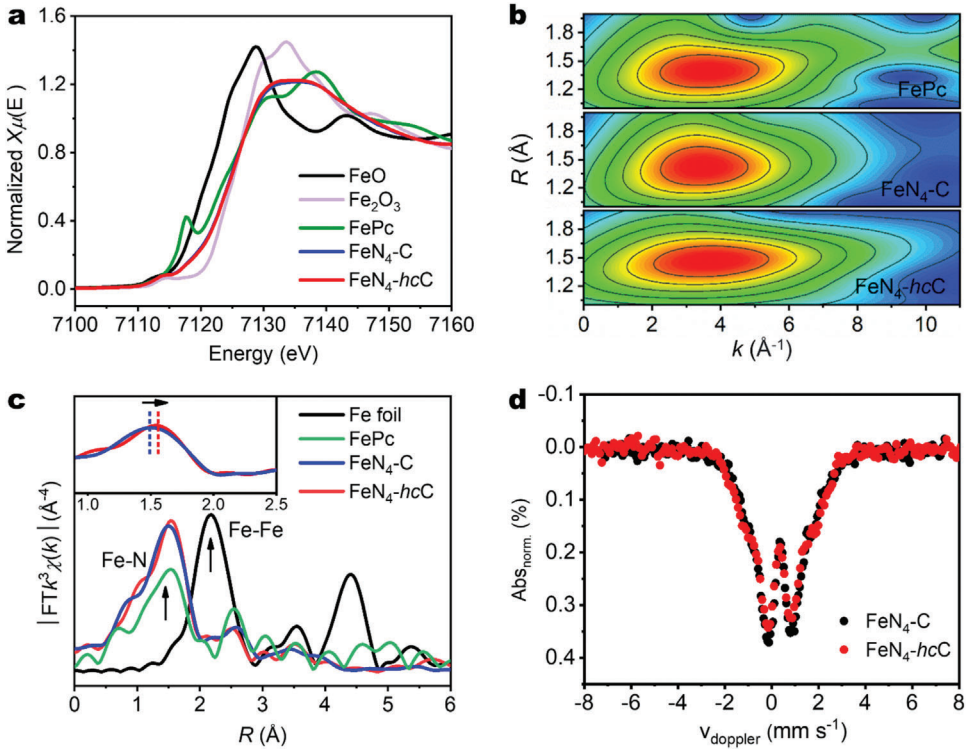

Figure 2. a) Fe *K*-edge XANES spectra. b) k^2-weighted wavelet transformed Fe *K*-edge EXAFS spectra and c) Fourier transformed Fe *K*-edge EXAFS spectra for FeN_4-C, FeN_4-*hc*C, and related reference compounds. d) Room-temperature ^{57}Fe Mössbauer spectrum of FeN_4-*hc*C and FeN_4-C (the absorption in the *y*-axis is normalized with the integrated area).

by the complete disappearance of the sharp peaks of ZIF-8 and the appearance of new broad peaks at ≈24.3° and ≈43.7°, assigning to the (002) and (101) planes of graphitic carbon. We then selected Fe-ZIF-8-550 and P123@Fe-ZIF-8-550 (pyrolyzed at 550 °C, still maintain the basic structure of ZIF-8) to prove the essential role of the P123. As shown in Figure S12 (Supporting Information), after heat treatment at 550 °C, the Fe-ZIF-8-550 still showed smooth surfaces. In sharp contrast, the P123@Fe-ZIF-8-550 exhibited rough surfaces, due to the promotional role of the P123. Thus, we proposed that the P123 induces the surface reconstruction of Fe-ZIF-8 at low temperatures and then promotes the arrangement of the Fe-ZIF-8 derived carbon during the high-temperature pyrolysis process, thus, promoting the formation of curved carbons on the surface FeN_4-*hc*C. At higher temperatures, the formation of Fe single atoms on nitrogen-doped carbon involved the ZIF-8 to carbon transformation, Zn evaporation, and Fe anchoring, as demonstrated in the previously reported results.[44] The Raman spectra of FeN_4-C and FeN_4-*hc*C displayed two peaks at ≈1350 and ≈1590 cm^{-1}, corresponding to the D band (disordered sp3 carbon) and G band (graphitic sp2 carbon) of graphitic carbon, respectively (Figure S13, Supporting Information).[45] Brunauer–Emmett–Teller (BET) analysis was used to determine the surface area of the FeN_4-*hc*C, which was found to be 733.9 m^2 g^{-1}, lower than the 810.7 m^2 g^{-1} value for FeN_4-C (Figure 1g; Figure S14 and Table S1, Supporting Information). ICP-OES measurements indicated a Fe content of 1.15 wt% in FeN_4-*hc*C, comparable to the 1.12 wt% content in FeN_4-C.

X-ray-based analyses, including XPS, X-ray absorption near-edge structure (XANES), and extended X-ray absorption fine structure (EXAFS), were used to determine the electronic environments and coordination information for FeN_4-C and FeN_4-*hc*C (Figures S15–S17, Supporting Information). The high-resolution N 1s XPS spectrum of FeN_4-*hc*C was deconvoluted into five peaks for N species, corresponding to pyridinic N (398.5 eV), Fe–N_x (399.2 eV), pyrrolic N (400.3 eV), graphitic N (401.0 eV), and oxidized N (402.7 eV)[35] (Figure S15, Supporting Information). The O contents in FeN_4-C and FeN_4-*hc*C were determined to be 5.1 and 5.3 at%, respectively, using XPS analysis. In the Fe *K*-edge XANES spectra, the absorption edges of FeN_4-C and FeN_4-*hc*C approached that of the standard Fe_2O_3, implying that the Fe in those samples was predominantly in the 3+ oxidation state[47] (**Figure 2**a). The wavelet-transformed (WT) EXAFS plots for FeN_4-C and FeN_4-*hc*C exhibited only one peak at ≈3.7 $Å^{-1}$ in *k* space, similar to Fe(II) phthalocyanine (FePc), suggesting an analogous first shell Fe–N coordination sphere[48] (Figure 2b). The WT EXAFS results indicated the presence of mononuclear Fe centers in FeN_4-C and FeN_4-*hc*C.[25] Fourier-transformed EXAFS (FT-EXAFS) spectra (Figure 2c) showed one dominant peak at ≈1.50 Å (without phase correction) for FeN_4-C and FeN_4-*hc*C, which was assigned to the first coordination shell scattering of the Fe–N bond.[49] A comparison with Fe foil indicated that there were no Fe–Fe bonds (≈2.2 Å) detected in FeN_4-C or FeN_4-*hc*C, further highlighting the single-atom natures of the Fe species in both systems. Interestingly, the average Fe–N bond distance in FeN_4-*hc*C was longer than that in FeN_4-C (inset of Figure 2c),

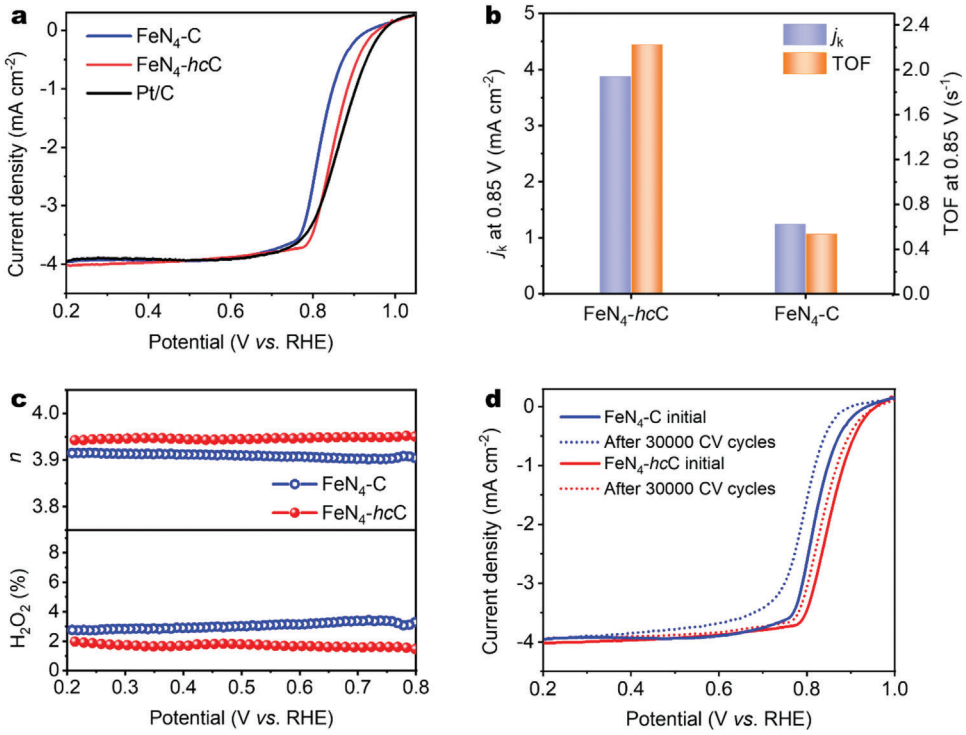

Figure 3. a) ORR polarization curves for FeN_4-*hc*C, FeN_4-C (0.6 mg cm^{-2}, 0.5 M H_2SO_4, 900 rpm) and Pt/C electrocatalysts (20%, 0.1 M $HClO_4$, 900 rpm). b) Mass activities and TOF values at 0.85 V and c) H_2O_2 yields and electron transfer numbers for the FeN_4-*hc*C and FeN_4-C electrocatalysts. d) ORR polarization curves for FeN_4-*hc*C and FeN_4-C before and after 30 000 CV cycles (in the potential range of 0.6–1.0 V, in O_2 saturated 0.5 M H_2SO_4 electrolyte, 900 rpm).

which was primarily attributed to the local strain effect of the curved onion-like carbons in FeN_4-*hc*C.[50,51] EXAFS quantitative fitting of the *R* space spectra was performed to resolve the first-shell coordination numbers and Fe–N bond distances in FeN_4-C and FeN_4-*hc*C. The well-fitted EXAFS results indicated that the single Fe sites in FeN_4-*hc*C and FeN_4-C contained Fe coordinated with four N atoms (Figure S17 and Table S2, Supporting Information). Room temperature (RT) ^{57}Fe Mössbauer spectra of FeN_4-*hc*C and FeN_4-C further supported the single-atom natures of the Fe sites in FeN_4-C and FeN_4-*hc*C.[52] The increase in Fe–N bond distance (seen in EXAFS) for FeN_4-*hc*C is also reflected by an increase in the central balance point of the overall Mössbauer spectrum (Figure 2d; Figure S18 and Table S3, Supporting Information). The above TEM, XANES, EXAFS, and RT-^{57}Fe Mössbauer analyses verified the successful construction of single metal FeN_4 sites in FeN_4-*hc*C.

The ORR performance of the FeN_4-*hc*C catalyst was assessed by utilizing linear sweep voltammetry (LSV) in an O_2-saturated 0.5 M H_2SO_4 electrolyte. FeN_4-C and Pt/C (in 0.1 M $HClO_4$, 60 μg cm^{-2}) were also evaluated for comparison. All potentials were referenced to the RHE. As displayed in **Figure 3**a, FeN_4-C exhibited considerable ORR performance with an $E_{1/2}$ of 0.82 V, which fell into a similar range reported for the Fe-modified ZIF-8-derived Fe–N–C materials (0.80–0.84 V; Table S4, Supporting Information). In contrast, the optimal FeN_4-*hc*C using 2 g of P123 in the synthesis process demonstrated greatly improved ORR performance with an $E_{1/2}$ of 0.85 V (Figure S19, Supporting Information), which approached that of the benchmark Pt/C ($E_{1/2}$ ≈ 0.86 V). The catalytic performance of FeN_4-*hc*C was comparable to that of the best-known Fe–N–C electrocatalysts (Table S4, Supporting Information). The kinetic current density (J_k) of FeN_4-*hc*C reached 3.87 mA cm^{-2} (6.45 A g_{cata}^{-1}) at 0.85 V, which was higher than the 1.23 mA cm^{-2} (2.05 A $g_{cata}.^{-1}$) value observed for FeN_4-C (Figure 3b; Figure S20, Supporting Information). A rotating ring-disk electrode (RRDE) was employed to quantify the ORR pathway.[53] As revealed in Figure 3c, the H_2O_2 yield of FeN_4-*hc*C was below 3.0% in the potential range of 0.2–0.8 V. The electron transfer number (*n*) was calculated to be >3.9, suggesting that the desired four-electron ORR process led to the formation of H_2O.[54] The intrinsic TOF value of FeN_4-*hc*C was determined by assessing the accessibility of the FeN_4 active sites, which was done with in situ electrochemical nitrite poisoning experiments[55] (Figure S21, Supporting Information). The calculation method is shown in the Supporting Information. Accordingly, the number of accessible FeN_4 active sites in FeN_4-*hc*C was determined to be 1.09×10^{19} sites g^{-1}, slightly lower than the 1.45×10^{19} site g^{-1} result for FeN_4-C. These results were consistent with the BET analysis, i.e., the higher BET surface area of FeN_4-C facilitates exposure of the single Fe sites. At the same time, the onion-like carbon structure may have partially inhibited the formation of the micropores allowing access to the FeN_4 sites. Based on the accessibility of the FeN_4 sites, the intrinsic turnover frequency (TOF) for FeN_4-*hc*C reached 2.22 s^{-1} at 0.85 V, which was ≈4.2 times higher than the 0.53 s^{-1} result for FeN_4-C (Figure 3b) and higher than those reported for Fe–N–C electrocatalysts (TOF values of <2.0 s^{-1} at 0.8 V; Table S5, Supporting

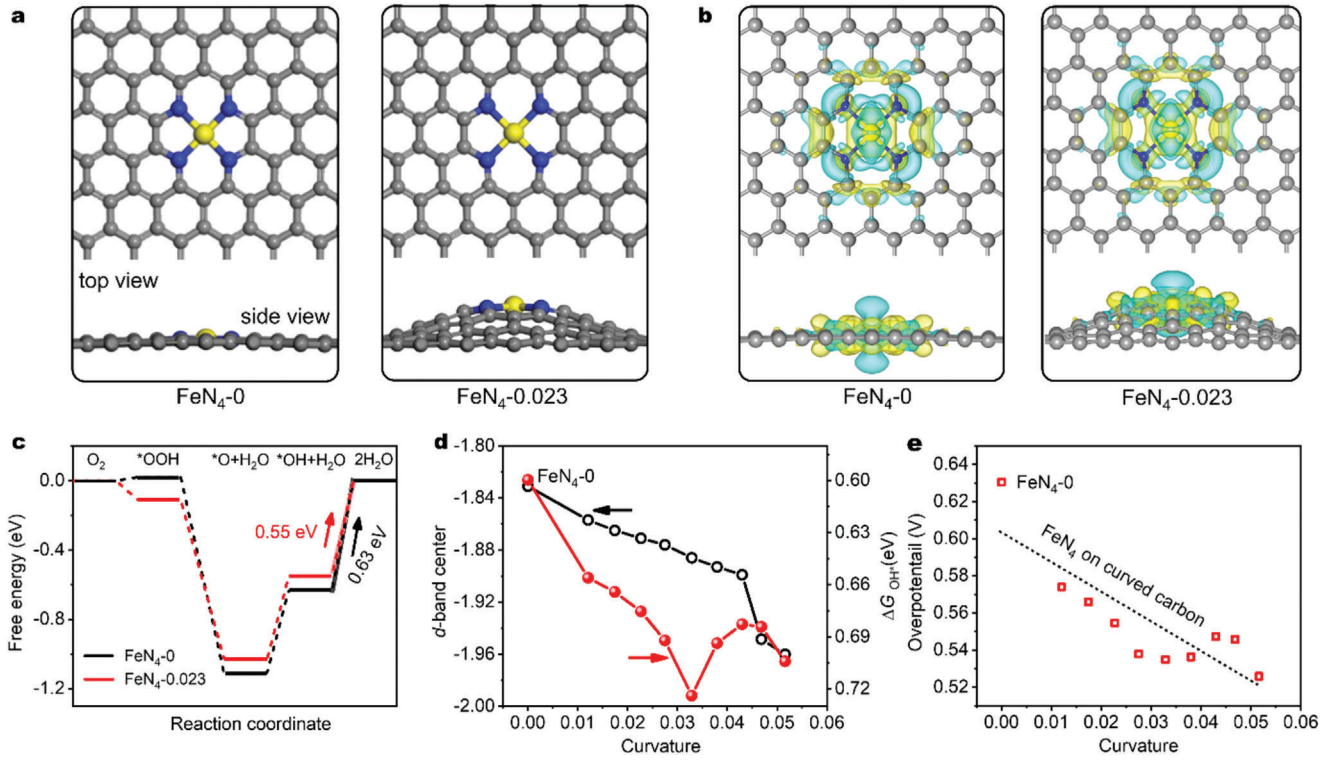

Figure 4. a) Schematic showing the FeN_4-0 and FeN_4-0.023 models. b) Charge density difference diagrams (yellow: electron accumulation; cyan: electron depletion) for FeN_4-0 and FeN_4-0.023. c) Gibbs free energy profiles for the ORR with FeN_4-0 and FeN_4-0.023 models at the equilibrium potential (U = 1.23 V). The arrows indicate the RDS. d,e) Correlations between the d-band center for the single Fe sites in FeN_4 and the ΔG_{OH^*} (d) and the ORR overpotential for FeN_4 with the curvature (e).

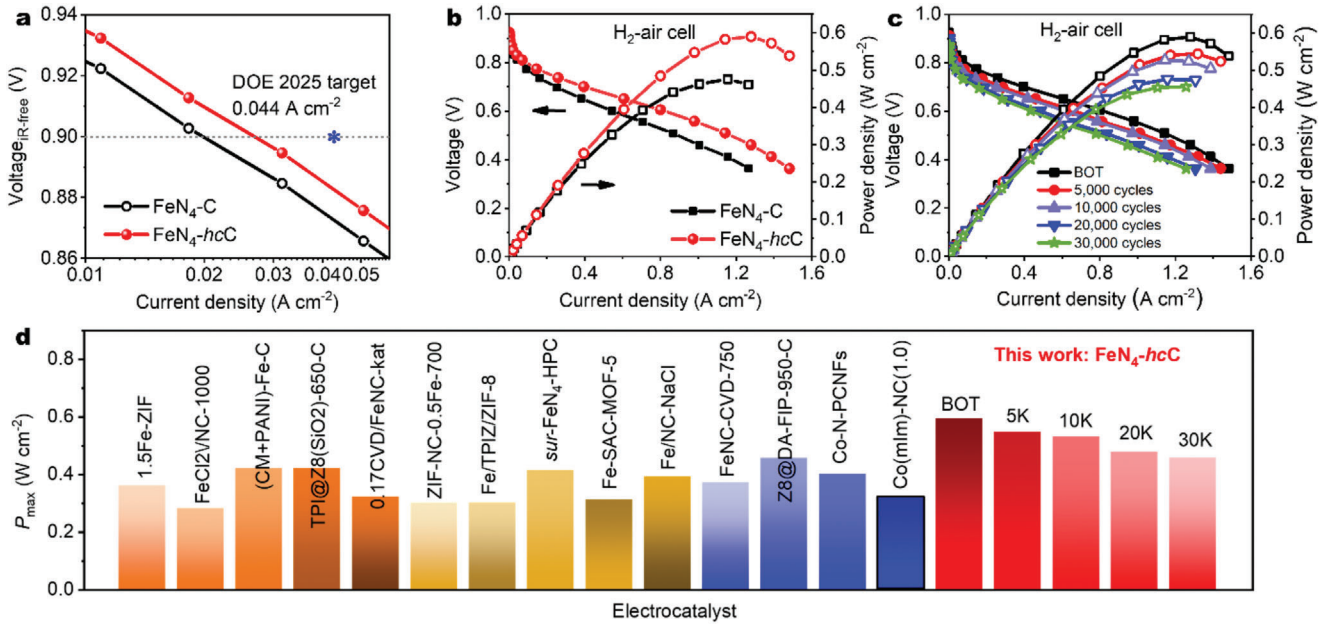

Figure 5. a) Polarization curves used for determining the mass activities of the FeN_4-C and FeN_4-*hc*C cathodes at 0.9 $V_{iR\text{-}free}$ and measured under 1.0 bar H_2–O_2 conditions. b) Polarization and power density curves for FeN_4-C and FeN_4-*hc*C in a 1.0 bar H_2–air PEMFC. c) Recorded polarization plots and power densities of the FeN_4-*hc*C cathode catalyst after different numbers of cycles. BOT stands for the beginning of the test. d) Performance comparison of the P_{max} value for the FeN_4-*hc*C cathode with those previously reported for M–N–C catalysts in H_2–air cells.

Information). The above results strongly suggested a higher average intrinsic FeN_4 activity for the ORR in FeN_4-*hc*C compared to that in FeN_4-C, which is largely probably due to the newly formed FeN_4 active sites on the highly curved carbon surfaces (i.e., on the onion-like nanocarbon surfaces). In addition, FeN_4-*hc*C exhibited excellent electrocatalytic durability, as evidenced by the minimal $E_{1/2}$ loss of only 19 mV after 30 000 cyclic voltammetry (CV) cycles (0.6–1.0 V), which was significantly lower than the losses for FeN_4-C (31 mV) (Figure 3d). The structural changes in FeN_4-*hc*C after the durability tests were examined by HRTEM and HAADF-STEM. Although a majority of curved carbons and single-atom structures were maintained, a few Fe aggregations were also detected. The number of accessible FeN_4 active sites in FeN_4-*hc*C after the stability test was determined to be 0.85×10^{19} site g^{-1}, slightly lower than that in the fresh FeN_4-*hc*C sample (Figure S22, Supporting Information). The Fe aggregations and the decreased FeN_4 site density are probably due to the carbon corrosion and dragging Fe atoms from the carbon skeleton. It has been demonstrated that the O content/hydrophilicity of the carbon-based materials might also affect the ORR activity.[56] In order to investigate these factors, we further prepared the controlled sample of FeN_4-C-F127 utilizing F127 ($(PEO_{100}–PPO_{65}–PEO_{100}$) as the surfactant and using F127@Fe-ZIF-8 as the corresponding precursor because F127 has the similar co-polymer units with that of P123.[57] As displayed in Figure S23 (Supporting Information), the F127@Fe-ZIF-8 (pyrolyzed at 1100 °C) derived FeN_4-C-F127 also inherited the morphology of ZIF-8. Compared with FeN_4-*hc*C, no curved carbons were observed on the surface of the FeN_4-C–F127 and densely single Fe atoms were detected. The O content in FeN_4-C–F127 was measured to be 5.4 at% using XPS analysis, slightly higher than that in FeN_4-C (5.1 at%) and FeN_4-*hc*C (5.3 at%). The Fe content was determined to be 1.13 wt% using ICP-OES measurement, similar to that in FeN_4-C (1.12 wt%) and FeN_4-*hc*C (1.15 wt%). All FeN_4-C, FeN_4-*hc*C, and FeN_4-C-F127 samples are super hydrophilic (water contact angle <25°; Figure S24, Supporting Information). The favorable hydrophilic surface would promote a better wetting of the electrode by the electrolyte, leading to an enhanced ORR activity because of the facilitated water/O_2 transfer and accessibility of catalytic active single Fe sites. We then compared the ORR activity of FeN_4-C, FeN_4-*hc*C and FeN_4-C-F127 in 0.5 M H_2SO_4. As revealed in Figure S25a (Supporting Information), FeN_4-*hc*C and FeN_4-C-F127 demonstrated higher ORR activity than that of FeN_4-C, suggesting the promotional effect of O content/hydrophilicity for ORR. However, the $E_{1/2}$ of FeN_4-C–F127 (0.83 V) was much lower than that of FeN_4-*hc*C (0.85 V) (Figure S25a, Supporting Information). In addition, the FeN_4-C–F127 showed inferior ORR stability than that of FeN_4-*hc*C, as evidenced by the larger $E_{1/2}$ loss (33 mV; Figure S25b, Supporting Information) after 30 000 CV cycles than that of FeN_4-*hc*C (19 mV; Figure 3d). The above results indicated that the O content/hydrophilicity could promote the ORR activity to a certain degree, but not the crucial factors. Therefore, we consider that the curved carbon nanostructure is the key factor for promoting both the ORR activity and stability for FeN_4-*hc*C.

Although it is challenging to count the percentages of single metal Fe sites on polyhedral carbons and the onion-like carbons in FeN_4-*hc*C with currently available techniques, the observed single Fe atoms on the highly curved onion-like carbons and the enhanced ORR activity of FeN_4-*hc*C inspired us to investigate the extent to which the curved carbon surfaces enhanced the intrinsic ORR activity. Accordingly, first principles DFT calculations were performed. Based on the above observations (onion-like carbon surfaces with diameters of ≈9 nm), we constructed a FeN_4 active site on a sp^2-hexagonal-carbon framework with a curvature (c) of 0.023, and the catalyst model was labeled as FeN_4-0.023. The FeN_4 sites on planer carbon surfaces ($c = 0$, FeN_4-0) were also considered for comparison (**Figure 4**a). Due to the instability of $FeN_{(pyrrolic)4}$ in acids,[30] in this work, we will focus mainly on the $FeN_{(pyridine)4}$ site. As shown in Table S6 (Supporting Information), the average Fe–N bond length in FeN_4-0.023 was 1.914 Å, which was obviously longer than that of the planar FeN_4-0 (1.892 Å). The bond length difference for FeN_4-0.023 and FeN_4-0 was consistent with the EXAFS result described above. The charge density difference plots show obvious charge transfer from the Fe center to the adjacent N atoms in both FeN_4-0 and FeN_4-0.023. Remarkably, the FeN_4-0.023 model induces more charge transfer than FeN_4-0 (Figure 4b). The d band center of FeN_4-0.023 was calculated to be −1.871, lower than the −1.831 value for FeN_4-0 (Table S6, Supporting Information). The downshifting in the d-band center in FeN_4-0.023 would weaken the adsorption ability of OH* intermediates and accelerate the overall ORR kinetics. Additionally, the Gibbs free energies were calculated to investigate the ORR process on FeN_4-0 and FeN_4-0.023. At a zero-electrode potential ($U = 0$ V vs RHE), both models exhibited a spontaneous exothermal process according to the downslope energy pathway[58] (Figure S26, Supporting Information). The ΔG_{OH^*} on FeN_4-0.023 was calculated to be 0.68 eV, higher than that of 0.60 eV calculated for FeN_4-0, which indicates that *OH moieties can more easily release on FeN_4-0.023 compared to FeN_4-0. At an applied voltage of 1.23 V (the ORR equilibrium potential), it can be observed in Figure 4c that the FeN_4-0 and FeN_4-0.023 owe the step of *OH desorption ($*OH + H^+ + e^- \rightarrow * + H_2O$) as the same rate-determining ORR step (RDS). The overpotential on FeN_4-0 was 0.63 V, while that on curved FeN_4-0.023 was 0.55 V, indicating faster ORR kinetics for the single metal FeN_4 sites on the curved carbon surfaces.

To further explore the correlation between the carbon curvature and the intrinsic activity of the FeN_4 sites, carbon frameworks with different curvatures (c = 0.012, 0.017, 0.023, 0.027, 0.033, 0.038, 0.043, 0.047, and 0.052) and supported single Fe sites were constructed (Table S6, Supporting Information), and the corresponding adsorption ability was calculated (Table S7, Supporting Information). As depicted in Figure 4d, with the increasing curvature of carbon, the d-band center of the single metal Fe sites in FeN_4 shift to the lower energy, subsequently reflecting the weaker interactions with OH* adsorbates and the lower ORR overpotential (Figure 4e; Figures S26 and S27 and Tables S6 and S7, Supporting Information). DFT calculations were also used to investigate the influence of curvature on the stability of the FeN_4 sites from the viewpoint of metal dissolution. The dissolution of FeN_4 sites was proposed to involve three sequential steps.[42] The two adjacent N atoms in a FeN_4 moiety are first protonated via adsorbed H^+ ions. During the ORR process, the central Fe atom usually adsorbs O_2 molecule. Resultantly, the co-adsorption of H^+ and O_2 on N and Fe atoms, respectively, can

lead to the cleavage of Fe–N bonds and the change of coordination environment from the N_4 coordination sphere to N_2 coordination. It significantly reduces the anchoring effect of N ligands on Fe atom and consequently, O_2 continues dragging Fe atoms from the carbon skeleton, resulting in FeN_4 deformation and dissolute into electrolytes. Therefore, the deformation of FeN_4 sites is the key to determining the stability of FeNC materials. As displayed in Table S6 and Figure S28 (Supporting Information), the free energy change for FeN_4 deformation (ΔG_d) in FeN_4-0 was calculated to be −1.35 V. In contrast, with the increasing curvature, a decrease in ΔG_d was found, which validated the enhanced stability of FeN_4 on the curved surface of the carbon. These DFT calculations demonstrated the following: 1) a higher curvature of the carbon results in higher intrinsic ORR activity and stability of the FeN_4 sites; 2) the curvature of the carbon surfaces in Fe–N–C materials could be an efficacious factor for ORR activity.

To evaluate the FeN_4-*hc*C catalyst in a practical PEMFC, the catalyst was incorporated into membrane electrode assemblies (MEAs) and investigated under fuel cell operating conditions. As shown in **Figure 5**a, FeN_4-*hc*C produced a mass activity of 26.9 mA cm^{-2} at 0.9 $V_{iR\text{-}free}$ under an O_2 partial pressure of 150 kPa_{abs}, higher than the 20.0 mA cm^{-2} value for FeN_4-C. This value was in the same range as those for the best-performing Fe–N–C materials (<30.0 mA cm^{-2} at 0.9 $V_{iR\text{-}free}$; Table S8, Supporting Information). Under practical 1.0 bar H_2–air conditions, FeN_4-*hc*C generated a current density of 92.6 mA cm^{-2} at 0.8 V, higher than the 72 mA cm^{-2} result for FeN_4-C. Moreover, the peak power density of the FeN_4-*hc*C cathode was 0.592 W cm^{-2}, higher than 0.473 W cm^{-2} for FeN_4-C (Figure 5b; Table S8, Supporting Information). After 30 000 accelerated stress test (AST) cycles, the peak power density for FeN_4-*hc*C was decreased by only 23.0% from 0.592 (beginning of the test (BOT)) to 0.456 W cm^{-2}) (Figure 5c; Figure S29a, Supporting Information). Notably, this value after 30 000 cycles was even higher than the BOT peak power densities of many previously reported Fe–N–C electrocatalysts (<0.45 W cm^{-2}; Figure 5d and Table S8, Supporting Information). At 0.65 V, the current density loss was 21.6% after 5000 AST cycles, and the accumulative decline was 54.3% after 30 000 AST cycles (from 603 to 276 mA cm^{-2}). At a lower voltage (i.e., 0.5 V), the current density losses were only 10.2% (from 1172 to 1053 mA cm^{-2}) and 31.2% (from 1172 to 806 mA cm^{-2}) after 5000 and 30 000 AST cycles, respectively (Figure S29b, Supporting Information). The fact that these performance metrics were retained in the harsh durability studies indicates the enormous potential of the FeN_4-*hc*C catalyst for long-term stability in PEMFCs.

3. Conclusions

We have demonstrated a novel FeN_4-*hc*C electrocatalyst with a dense population of single FeN_4 sites on a hierarchically porous carbon with highly curved surfaces. This electrocatalyst was prepared via a P123-mediated synthetic method. The resulting FeN_4-*hc*C catalyst displayed outstanding ORR performance in acidic media. In addition, FeN_4-*hc*C exhibited superior activity in a practical PEMFC device, comparable to the state-of-the-art Fe–N–C materials known to date. Our experimental results and theoretical calculations suggested that the curved carbon surface enhanced the intrinsic activity of the single metal FeN_4 site by tailoring the electronic structure of the single Fe center, weakening its interaction with OH*, and reducing the FeN_4 deformation. The construction of hierarchically porous carbons with highly curved carbon surfaces presented in this work can guide explorations of highly effective single-metal-site electrocatalysts for many other energy conversion reactions, e.g., water splitting, CO_2 reduction, and N_2 reduction.

Supporting Information

Supporting Information is available from the Wiley Online Library or from the author.

Acknowledgements

G.C. and R.L. contributed equally to this work. The authors thank the funding supports from the European Research Council (ERC) under the European Union's Horizon 2020 research and Innovation Programme (Grant Agreement No. 819698 and GrapheneCore3: 881603), Deutsche Forschungsgemeinschaft (COORNETs, SPP 1928 and CRC 1415: 417590517). U.I.K. and L.N. acknowledge financial support by the BMBF young researcher group (03XP0092) and the DFG-funding via CRC 1487, *Iron, upgraded!* (Project No. 443703006). G.W. acknowledges the financial support from the U.S. Department of Energy, Hydrogen and Fuel Cell Technologies Office (DE–EE0008075, DE–EE0008076, and DE–EE0008417). The authors also acknowledge the Center for Advancing Electronics Dresden (Cfaed) and the Dresden Center for Nanoanalysis (DCN) at TU Dresden.

Open access funding enabled and organized by Projekt DEAL.

Conflict of Interest

The authors declare no conflict of interest.

Data Availability Statement

The data that support the findings of this study are available from the corresponding author upon reasonable request.

Keywords

carbon curvature, Fe–N–C catalysts, fuel cells, hierarchically porous carbons, oxygen reduction reaction

Received: January 30, 2023
Revised: April 28, 2023
Published online:

[1] E. L. Miller, S. T. Thompson, K. Randolph, Z. Hulvey, N. Rustagi, S. Satyapal, *MRS Bull.* **2020**, *45*, 57.
[2] Y. Jiao, Y. Zheng, M. Jaroniec, S. Z. Qiao, *Chem. Soc. Rev.* **2015**, *44*, 2060.
[3] T. Asset, P. Atanassov, *Joule* **2020**, *4*, 33.
[4] C. Zhu, H. Li, S. Fu, D. Du, Y. Lin, *Chem. Soc. Rev.* **2016**, *45*, 517.
[5] M. Shao, Q. Chang, J.-P. Dodelet, R. Chenitz, *Chem. Rev.* **2016**, *116*, 3594.
[6] K. Jiao, J. Xuan, Q. Du, Z. Bao, B. Xie, B. Wang, Y. Zhao, L. Fan, H. Wang, Z. Hou, S. Huo, N. P. Brandon, Y. Yin, M. D. Guiver, *Nature* **2021**, *595*, 361.

[7] R. Haider, Y. Wen, Z.-F. Ma, D. P. Wilkinson, L. Zhang, X. Yuan, S. Song, J. Zhang, *Chem. Soc. Rev.* **2021**, *50*, 1138.
[8] F. Xiao, Y.-C. Wang, Z.-P. Wu, G. Chen, F. Yang, S. Zhu, K. Siddharth, Z. Kong, A. Lu, J.-C. Li, C.-J. Zhong, Z.-Y. Zhou, M. Shao, *Adv. Mater.* **2021**, *33*, 2006292.
[9] J. Yan, F. Ye, Q. Dai, X. Ma, Z. Fang, L. Dai, C. Hu, *Nano Res. Energy* **2023**, *2*, e9120047.
[10] X. Xie, L. Shang, X. Xiong, R. Shi, T. Zhang, *Adv. Energy Mater.* **2022**, *12*, 2102688.
[11] X. Xie, L. Peng, H. Yang, G. I. N. Waterhouse, L. Shang, T. Zhang, *Adv. Mater.* **2021**, *33*, 2101038.
[12] A. Mehmood, M. Gong, F. Jaouen, A. Roy, A. Zitolo, A. Khan, M.-T. Sougrati, M. Primbs, A. M. Bonastre, D. Fongalland, G. Drazic, P. Strasser, A. Kucernak, *Nat. Catal.* **2022**, *5*, 311.
[13] X. X. Wang, M. T. Swihart, G. Wu, *Nat. Catal.* **2019**, *2*, 578.
[14] S. Ji, Y. Chen, X. Wang, Z. Zhang, D. Wang, Y. Li, *Chem. Rev.* **2020**, *120*, 11900.
[15] L. Du, V. Prabhakaran, X. Xie, S. Park, Y. Wang, Y. Shao, *Adv. Mater.* **2021**, *33*, 1908232.
[16] Q. Miao, S. Yang, Q. Xu, M. Liu, P. Wu, G. Liu, C. Yu, Z. Jiang, Y. Sun, G. Zeng, *Small Struct.* **2022**, *3*, 2100225.
[17] Y. He, S. Liu, C. Priest, Q. Shi, G. Wu, *Chem. Soc. Rev.* **2020**, *49*, 3484.
[18] H. Zhang, H. T. Chung, D. A. Cullen, S. Wagner, U. I. Kramm, K. L. More, P. Zelenay, G. Wu, *Energy Environ. Sci.* **2019**, *12*, 2548.
[19] E. Luo, Y. Chu, J. Liu, Z. Shi, S. Zhu, L. Gong, J. Ge, C. H. Choi, C. Liu, W. Xing, *Energy Environ. Sci.* **2021**, *14*, 2158.
[20] D. Menga, J. L. Low, Y.-S. Li, I. Arčon, B. Koyutürk, F. Wagner, F. Ruiz-Zepeda, M. Gaberšček, B. Paulus, T.-P. Fellinger, *J. Am. Chem. Soc.* **2021**, *143*, 18010.
[21] T. Sun, S. Mitchell, J. Li, P. Lyu, X. Wu, J. Pérez-Ramírez, J. Lu, *Adv. Mater.* **2021**, *33*, 2003075.
[22] L. Yang, D. Cheng, H. Xu, X. Zeng, X. Wan, J. Shui, Z. Xiang, D. Cao, *Proc. Natl. Acad. Sci. USA* **2018**, *115*, 6626.
[23] G.-F. Han, F. Li, A. I. Rykov, Y.-K. Im, S.-Y. Yu, J.-P. Jeon, S.-J. Kim, W. Zhou, R. Ge, Z. Ao, T. J. Shin, J. Wang, H. Y. Jeong, J.-B. Baek, *Nat. Nanotechnol.* **2022**, *17*, 403.
[24] H. T. Chung, D. A. Cullen, D. Higgins, B. T. Sneed, E. F. Holby, K. L. More, P. Zelenay, *Science* **2017**, *357*, 479.
[25] X. Wan, X. Liu, Y. Li, R. Yu, L. Zheng, W. Yan, H. Wang, M. Xu, J. Shui, *Nat. Catal.* **2019**, *2*, 259.
[26] A. Zitolo, V. Goellner, V. Armel, M.-T. Sougrati, T. Mineva, L. Stievano, E. Fonda, F. Jaouen, *Nat. Mater.* **2015**, *14*, 937.
[27] C. Zhu, Q. Shi, B. Z. Xu, S. Fu, G. Wan, C. Yang, S. Yao, J. Song, H. Zhou, D. Du, S. P. Beckman, D. Su, Y. Lin, *Adv. Energy Mater.* **2018**, *8*, 1801956.
[28] H. Adabi, A. Shakouri, N. Ul Hassan, J. R. Varcoe, B. Zulevi, A. Serov, J. R. Regalbuto, W. E. Mustain, *Nat. Energy* **2021**, *6*, 834.
[29] L. Jiao, J. Li, L. L. Richard, Q. Sun, T. Stracensky, E. Liu, M. T. Sougrati, Z. Zhao, F. Yang, S. Zhong, H. Xu, S. Mukerjee, Y. Huang, D. A. Cullen, J. H. Park, M. Ferrandon, D. J. Myers, F. Jaouen, Q. Jia, *Nat. Mater.* **2021**, *20*, 1385.
[30] J. Li, M. T. Sougrati, A. Zitolo, J. M. Ablett, I. C. Oğuz, T. Mineva, I. Matanovic, P. Atanassov, Y. Huang, I. Zenyuk, A. Di Cicco, K. Kumar, L. Dubau, F. Maillard, G. Dražić, F. Jaouen, *Nat. Catal.* **2021**, *4*, 10.
[31] L. Liu, A. Corma, *Chem. Rev.* **2018**, *118*, 4981.
[32] L. Ni, C. Gallenkamp, S. Wagner, E. Bill, V. Krewald, U. I. Kramm, *J. Am. Chem. Soc.* **2022**, *144*, 16827.
[33] L. Du, L. Xing, G. Zhang, M. Dubois, S. Sun, *Small Methods* **2020**, *4*, 2000016.
[34] M. Xiao, Y. Chen, J. Zhu, H. Zhang, X. Zhao, L. Gao, X. Wang, J. Zhao, J. Ge, Z. Jiang, S. Chen, C. Liu, W. Xing, *J. Am. Chem. Soc.* **2019**, *141*, 17763.
[35] G. Chen, Y. An, S. Liu, F. Sun, H. Qi, H. Wu, Y. He, P. Liu, R. Shi, J. Zhang, A. Kuc, U. Kaiser, T. Zhang, T. Heine, G. Wu, X. Feng, *Energy Environ. Sci.* **2022**, *15*, 2619.
[36] Y. He, G. Wu, *Acc. Mater. Res.* **2022**, *3*, 224.
[37] L. Wang, X. Wan, S. Liu, L. Xu, J. Shui, *J. Energy Chem.* **2019**, *39*, 77.
[38] U. I. Kramm, J. Herranz, N. Larouche, T. M. Arruda, M. Lefèvre, F. Jaouen, P. Bogdanoff, S. Fiechter, I. Abs-Wurmbach, S. Mukerjee, J.-P. Dodelet, *Phys. Chem. Chem. Phys.* **2012**, *14*, 11673.
[39] Q. Wang, L. Shang, D. Sun-Waterhouse, T. Zhang, G. Waterhouse, *SmartMat* **2021**, *2*, 154.
[40] K. Liu, G. Wu, G. Wang, *J. Phys. Chem. C* **2017**, *121*, 11319.
[41] Y. Shao, J.-P. Dodelet, G. Wu, P. Zelenay, *Adv. Mater.* **2019**, *31*, 1807615.
[42] S. Liu, C. Li, M. J. Zachman, Y. Zeng, H. Yu, B. Li, M. Wang, J. Braaten, J. Liu, H. M. Meyer, M. Lucero, A. J. Kropf, E. E. Alp, Q. Gong, Q. Shi, Z. Feng, H. Xu, G. Wang, D. J. Myers, J. Xie, D. A. Cullen, S. Litster, G. Wu, *Nat. Energy* **2022**, *7*, 652.
[43] J. Scharf, M. Kübler, V. Gridin, W. D. Z. Wallace, L. Ni, S. D. Paul, U. I. Kramm, *SusMat* **2022**, *2*, 630.
[44] H. Zhang, S. Hwang, M. Wang, Z. Feng, S. Karakalos, L. Luo, Z. Qiao, X. Xie, C. Wang, D. Su, Y. Shao, G. Wu, *J. Am. Chem. Soc.* **2017**, *139*, 14143.
[45] J. Zhang, Z. Zhao, Z. Xia, L. Dai, *Nat. Nanotechnol.* **2015**, *10*, 444.
[46] Z. Liang, N. Kong, C. Yang, W. Zhang, H. Zheng, H. Lin, R. Cao, *Angew. Chem., Int. Ed.* **2021**, *60*, 12759.
[47] J. Gu, C.-S. Hsu, L. Bai, H. M. Chen, X. Hu, *Science* **2019**, *364*, 1091.
[48] Z. Miao, X. Wang, Z. Zhao, W. Zuo, S. Chen, Z. Li, Y. He, J. Liang, F. Ma, H.-L. Wang, G. Lu, Y. Huang, G. Wu, Q. Li, *Adv. Mater.* **2021**, *33*, 2006613.
[49] X. Fu, N. Li, B. Ren, G. Jiang, Y. Liu, F. M. Hassan, D. Su, J. Zhu, L. Yang, Z. Bai, Z. P. Cano, A. Yu, Z. Chen, *Adv. Energy Mater.* **2019**, *9*, 1803737.
[50] Z. Zhu, N. Wei, J. Gao, Y. Jiang, L. Peng, F. Wei, *J. Appl. Phys.* **2021**, *129*, 025107.
[51] M. S. Dresselhaus, A. Jorio, M. Hofmann, G. Dresselhaus, R. Saito, *Nano Lett.* **2010**, *10*, 751.
[52] U. I. Kramm, L. Ni, S. Wagner, *Adv. Mater.* **2019**, *31*, 1805623.
[53] Z. Jin, P. Li, Y. Meng, Z. Fang, D. Xiao, G. Yu, *Nat. Catal.* **2021**, *4*, 615.
[54] M. Qiao, Y. Wang, Q. Wang, G. Hu, X. Mamat, S. Zhang, S. Wang, *Angew. Chem., Int. Ed.* **2020**, *59*, 2688.
[55] D. Malko, A. Kucernak, T. Lopes, *Nat. Commun.* **2016**, *7*, 13285.
[56] L. Yang, J. Shui, L. Du, Y. Shao, J. Liu, L. Dai, Z. Hu, *Adv. Mater.* **2019**, *31*, 1804799.
[57] L. Peng, H. Peng, Y. Liu, X. Wang, C.-T. Hung, Z. Zhao, G. Chen, W. Li, L. Mai, D. Zhao, *Sci. Adv.* **2021**, *7*, eabi7403.
[58] J. K. Nørskov, J. Rossmeisl, A. Logadottir, L. Lindqvist, J. R. Kitchin, T. Bligaard, H. Jónsson, *J. Phys. Chem. B* **2004**, *108*, 17886.